A Megawatt-Class Electrical Machine Technology Demonstrator For Turbo-Electric Propulsion

A Megawatt-Class Electrical Machine Technology Demonstrator For Turbo-Electric Propulsion

Zoltán S. Spakovszky*, Yuankang Chen†, Edward M. Greitzer‡, Zachary C. Cordero§, Jeffrey H. Lang¶, James L. Kirtley, Jr.‖, David J. Perreault**, Henry N. Andersen††, Mohammad M. Qasim‡‡, David G. Cuadrado§§, David M. Otten¶¶, and Marc Amato***
Massachusetts Institute of Technology, Gas Turbine Laboratory, Cambridge, MA, 02139

While continued propulsion system and turbomachinery improvements are necessary, they are not sufficient to address the 2050 aviation sustainability goals. Without intervention aviation will emit a cumulative total of over 20 billion tons of CO_2 by then. An ambitious target is to achieve a net-zero economy by 2050. The step change achievements needed to address the climate grand challenge are unconventional aircraft configurations with integrated and distributed propulsion systems, thermal management of high power-density rotating machinery, advanced high temperature materials, reduced, but safe, engineering and operability margins for improved performance, alternative energy carriers, smart and flexible fuel systems, and key enabling technology demonstrations. Independent of the energy carrier (battery, SAF, H_2, NH_3), MW class electrical machines will play a key role in greening aviation. To address the climate and sustainability grand challenge, a high specific power fully air-cooled 1 MW electrical machine is being developed, conceived to advance electrified aviation but also suitable for other ground-based applications. One application is integration in an aero-engine as a motor-drive for turbo-electric propulsion. The emphasis of this project is on risk mitigation experiments and technology demonstration of a 1 MW integrated motor drive with performance estimates exceeding the NASA 2030 goals.

I. Nomenclature

P	=	power
m	=	mass
Ξ	=	specific power
χ	=	hub-to-tip radius ratio
l	=	machine length
t_w	=	winding thickness
h_o	=	active element thickness
g	=	airgap thickness
r_{ag}	=	airgap radius
Ω	=	mechanical speed
U_{ag}	=	airgap speed
B_c	=	core saturation flux density
μ_0	=	permeability of free space

*T. A. Wilson Professor in Aeronautics; Head, Air Sector; Director, Gas Turbine Laboratory, 31-317
†Research Assistant, now working at GE Global Research
‡H.N. Slater Professor of Aeronautics and Astronautics, 31-319
§Assistant Professor of Aeronautics and Astronautics, 33-332
¶Vitesse Professor of Electrical Engineering, 10-176
‖Professor of Electrical Engineering (Post-Tenure), 10-098
**Ford Foundation Professor of Engineering, 10-039
††Graduate Research Assistant, EECS, 31-304
‡‡Doctoral Candidate, EECS, 10-026
§§Research Engineer, 31-316
¶¶Principal Research Engineer, Research Laboratory of Electronics, 10-039
***CEO,Innova-Logic LLC, Saunderstown, RI, 02874

K_s = surface current density
J_m = slot current density
τ = electromagnetic shear stress*
ρ_m = mass density
p = pressure
T = temperature
M = Mach number

II. Introduction

Aviation's annual share of global CO_2 emissions is over 1 billion tons of CO_2 and a large number of research collaborations and industry and government efforts are on their way to address the climate grand challenge. Among these is electrification of aviation which requires high efficiency and high specific power electrical machines and drive systems. For small general aviation type aircraft with power requirements of hundreds of kWs, electric motors and generators have already been successfully demonstrated. A main challenge is the development of MW-class electrical machines and power electronics to electrify single- and twin-aisle aircraft which make up the majority of total fuel consumption and thus emissions. One concept is the NASA STARC-ABL single aisle aircraft with a turbo-electric propulsion system. With present day gas turbine and airframe technology this concept could yield a 7-12% reduction in fuel burn[1]. Realizing this reduction requires significant improvements in specific power of the electric drivetrain components (the motors, generators, and power electronics), with target specific power of 13 kW/kg for electric machines and 16 kW/kg for the power electronics. The latter number refers specifically to AC-to-DC or DC-to-AC converters only. This number would be halved for an AC-to-AC converter.

A survey of present-day high specific power electric machines[2] shows a maximum specific power of 8.5 kW/kg at the low kW range and falls off with the inverse of the square root of rated power ([3]). Given the multi-megawatt power requirements of single- and twin-aisle aircraft a paradigm shift in electrical machine performance is required. This is indicated by the red area in Figure 1).

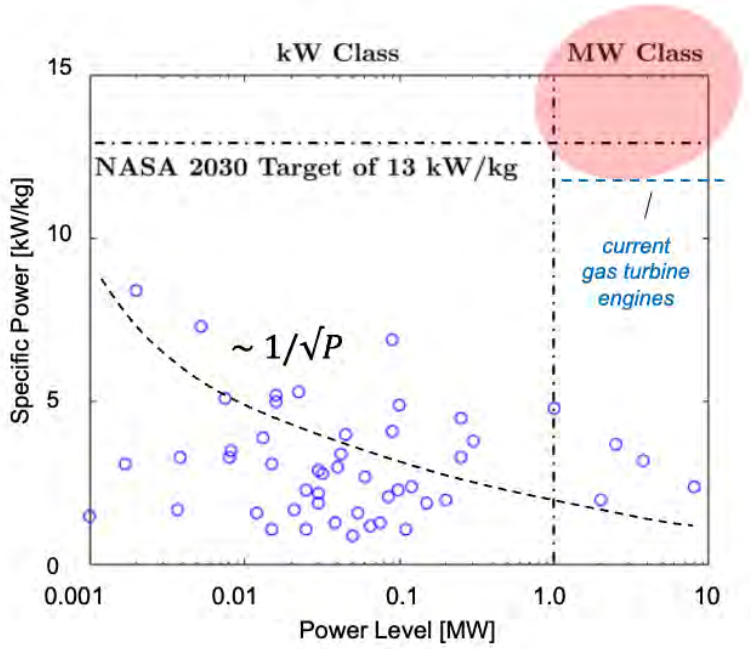

Fig. 1 A paradigm shift in electrical machine performance is required to enable MW-class electrical machines for turbo-electric propulsion. Blue circles are existing machines from survey data [2]

*Electromagnetic shear stress is the product of the magnetic flux density (B_s) from the rotor and the surface current density (K_s) from the stator windings: $\bar{\tau} = \frac{B_s K_s}{2}$

Similarly, typical best-in-class commercially-available multi-megawatt power electronics [4] have specific powers of 2-3 kW/kg as shown in Fig. 2 and a leap in performance is required to meet the NASA goal of 7.5 kW/kg for full AC/AC converters. The performance requirement for AC/DC converters is twice this number as mentioned above.

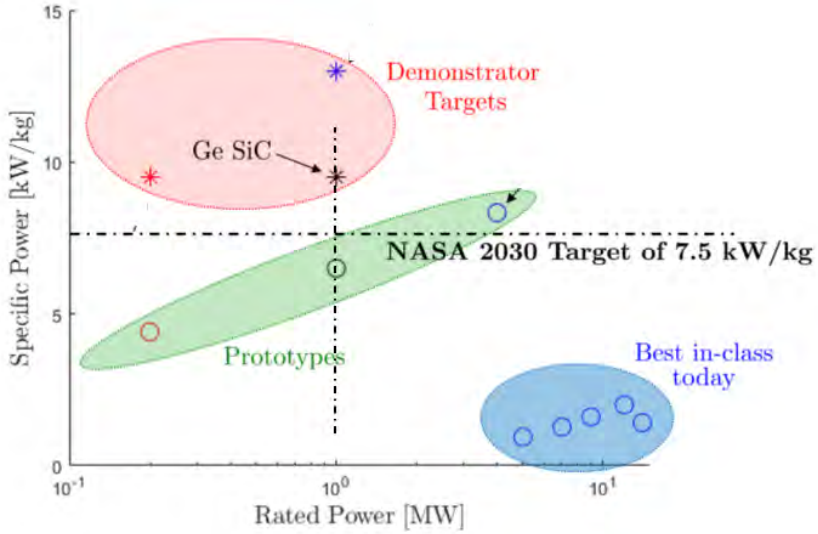

Fig. 2 Relative to the best in-class power electronics [4] a leap in performance is required to meet the goals of electrified aviation. The NASA target value of 7.5 kW/kg is for AC/AC converters - the target value for AC/DC converters is 16 kW/kg.

Considering a turbo-electric propulsion system configuration with an electrical machine embedded in the compression system of a gas turbine aero-engine, the functional requirements for the electrical machine and power electronics include (1) an outer rotor architecture for integration with the turbomachinery, (2) air cooling compatible with the air-breathing gas turbine based propulsion system, (3) compact, integrated power electronics for high-specific power and efficiency, (4) compatibility with typical aero-engine materials and manufacturing, and (5) engine operability encompassing aero-electro-mechanical and rotordynamic stability.

The architecture and topology of a high specific power electrical machine with integrated power electronics is identified via a combination of physics-based scaling laws and an extensive design space exploration. Starting with the scaling laws and an introduction to the design co-optimization (the details can be found in [5] and [3]), this paper gives an overview of the design and technology demonstration of a fully air-cooled 1 MW integrated motor drive. An outer rotor Halbach Array with a tooth-and-slot stator is selected for the electric machine architecture, and a full-bridge single-phase architecture for the power electronics. Illustrated in Fig. 3 four technologies are identified as critical to a high performance motor drive, each discussed in more detail in companion papers:

- **High-Speed Halbach-Array Rotor:** A lightweight load-bearing rotor rim is used to retain the magnets, and is sized to support their centrifugal loads. The rotor must possess sufficient stiffness to maintain the electric machine air gap when crossing rigid body modes [6].

- **Compact, Low Loss Tooth-and-Slot Stator:** To maximize specific power, the electric machine is designed for operation at high electrical frequency and with the core close to saturation. Minimization of the fundamental frequency core losses and high frequency losses imposed by the pulse-width modulation waveforms is critical to keeping hotspot temperature within limits[7].

- **Load-Bearing Heat Sink:** The heat exchanger of the electric machine is used as a structural element, transmitting torque from the machine stator to the frame. In addition to low stagnation pressure drop and high cooling

effectiveness, the heat exchanger must also meet stringent structural integrity requirements [8].

- **Close-coupled Distributed Power Electronics:** Distributed power conversion is key to achieving an integrated motor drive with high specific power and efficiency. Close coupling of the machine and electronics via physical integration reduces over-voltage and line reflections, minimizes losses, weight and EMI filter requirements [9].

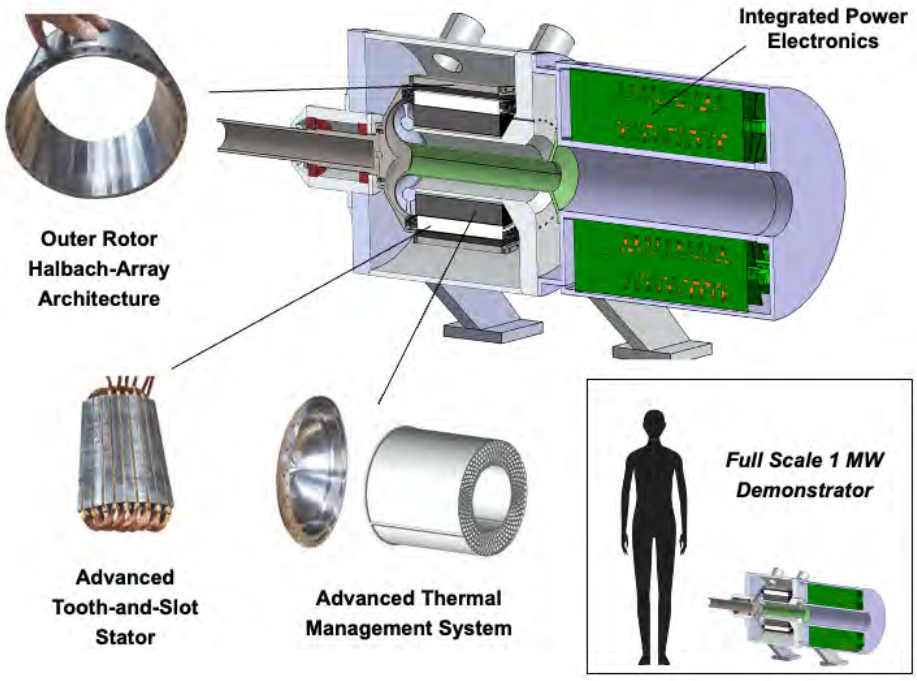

Fig. 3 Full scale 1 MW motor drive demonstrator with focus on key enabling technologies: a high-speed Halbach-array outer rotor, a low loss tooth-and-slot stator, a load-bearing heat sink, and closely coupled high-performance power electronics.

The technical challenges are multi-disciplinary and encompass a wide range of items such as high surface speed and electromagnetic shear stress, structural integrity of the magnetic rotor, torque transfer through the heat sink, mitigation of torque ripple, tight control of the running clearances, stable supercritical rotordynamic operation, high drive-switching frequency, stator stack fabrication with ultra-thin laminations, a high copper fill factor, robust insulation of the windings, differential thermal growth of key components, and thermal management.

A fully air-cooled 1 MW integrated motor drive is developed to demonstrate the viability of the identified architectures and technologies. The design parameters are selected through a co-optimization process, where the motor drive is optimized as an integrated system, accounting for masses and losses of the electric machine, power electronics, structure, and thermal management system. Accounting for the weight of the electric machine, power converter system, thermal management system, and supporting structure, the specific power of the overall motor drive is estimated at 10.5 kW/kg. This exceeds the NASA target of 7.2 kW/kg based on combining a 13 kW/kg electrical machine with 16 kW/kg power electronics. The specific power of the present electrical machine plus thermal management and the power electronics plus air cooling are estimated to be 17 kW/kg and 20 kW/kg respectively. Two identical motor drives are being built and will be commissioned in a back-to-back configuration, with experimental investigations into transient behavior and control strategies planned.

III. Electric Machine Scaling Laws

A. Radial-Flux Machines

The basis of the scaling laws for electric machines discussed next can be found in Smith et al. [10], and apply specifically to radial flux machines, where the rotor is radially inward or outward of the stator. Torque on the electric machine rotor is the product of an average electromagnetic shear stress $\bar{\tau}$, the area of the electromagnetic shear interface along which $\bar{\tau}$ acts (as illustrated in Figure 4), and the radius of this interface, also defined in literature as the air gap radius. The tip radius of the electric machine is defined here as the radius of the electromagnetic shear interface, and the air gap thickness is assumed to be significantly smaller than the tip radius of the electric machine $g/r << 1$.

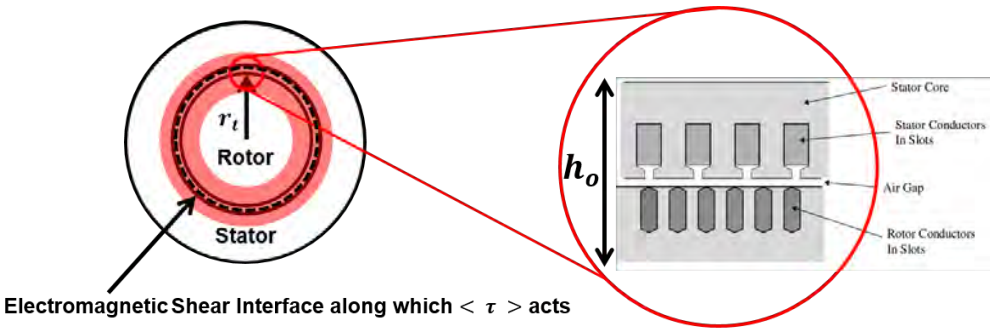

Fig. 4 Idealized hoop motor for scaling law analysis [10]

Electromagnetic shear stress is the product of the magnetic flux density (B_s) from the rotor and the surface current density (K_s) from the stator windings. In electric machines which prioritize efficiency, $\bar{\tau}$ ranges from 5 kPa in small machines (kilowatt level) to 100 kPa for large, well-cooled machines (gigawatt level). Machines with high specific torque requirements can approach the theoretical shear stress limit. At the cost of reduced efficiency and substantial cooling loads, the Cheetah motor [11] has an electromagnetic shear stress of $\bar{\tau} = 180$ kPa.

The power output of the electric machine can be written as

$$P_E = T\Omega = \bar{\tau}(2\pi r_{ag} l) r_{ag} \Omega = 2\pi \frac{l}{r_{ag}} \bar{\tau} \mathbf{r_{ag}^3 \Omega}. \tag{1}$$

The electromagnetic shear stress is generated by the active elements of the machine, illustrated in Figure 4 as the combination of stator core, stator conductors, rotor conductors, and rotor core, with total thickness h_o. These conductors can be either electromagnets (windings) or magnets. The mass of the electric machine then becomes

$$m_E = \rho_{m,E} 2\pi r_{ag} l h_o = \rho_E 2\pi \frac{l}{r_{ag}} \frac{h_o}{r_{ag}} \mathbf{r_{ag}^3}, \tag{2}$$

where $\rho_{m,E}$ is the average mass density of the active elements. The specific power of the electric machine can then be expressed as

$$\frac{P_E}{m_E} = \frac{\bar{\tau}\Omega}{\rho_{m,E} \frac{h_o}{r_{ag}}}, \tag{3}$$

which illustrates the four key parameters that drive electric machine specific power: electromagnetic shear stress $\bar{\tau}$, mechanical speed Ω, active element mass density $\rho_{m,E}$, and active element spatial density $\frac{h_o}{r_{ag}}$.

1. Specific Power Scaling with Rated Power

An alternative expression can be derived for specific power by recognizing that the mechanical stresses in the rotor scale with **airgap speed** U_{ag} (the product of airgap radius and mechanical speed):

$$\frac{P_E}{m_E} = \sqrt{2\pi} \frac{\bar{\tau}^{1.5} {U_{ag}}^{1.5} (\frac{l}{r_{ag}})^{0.5}}{\rho_{m,E} (\frac{h_o}{r_{ag}})} \frac{1}{\sqrt{P_E}}. \tag{4}$$

This expression for the specific power captures the constraints on the electric machine design and the scaling with machine rated power. To first order, electric machines designed at their performance limits will see specific power scale with the inverse of the square root of rated power.

Electromagnetic shear stress is the product of the magnetic flux density (B_s) from the rotor and the surface current density (K_s) from the stator windings [10]:

$$\bar{\tau} = \frac{B_s K_s}{2}. \tag{5}$$

In a permanent magnet machine with a specified magnetic material (e.g. Neodymium), the magnetic flux density can be increased with magnet thickness at the cost of higher magnet losses and rotor mechanical stresses (related to containing the centrifugal forces imposed by the magnets). Surface current density can be increased with slot current density J_m and winding thickness t_w. Increasing slot current density directly increases copper losses, while a larger winding thickness increases machine mass and radial thermal resistance of the windings (increasing the difficulty of cooling the windings).

Increasing tip speed comes at the cost of increased rotor mechanical stresses, windage losses, and unbalance forces. The rotordynamic operability of the electric machine is also a critical constraint at high speeds, as the difficulty of keeping the rotor whirl radius below the small air gaps required become increasingly difficult.

Machine aspect ratio is constrained by a combination of rotordynamic and thermal management. A high aspect ratio yields long and slender rotors with lower critical speeds, which makes maintaining the machine air gap in operation challenging. A high aspect ratio also increases the thermal management challenge as the surface area to volume ratio falls.

The choice of active element mass density and volumetric density are governed material limitations. Rare-earth magnet materials (such as neodymium and samarium-cobalt) would produce the same electromagnetic shear stress as their ceramic counterparts with less magnet thickness, thus improving the active element volumetric density. Similarly, for neodymium and samarium-cobalt magnets with comparable remnant flux, the reduced mass density of the neodymium magnet would improve the specific power of the machine.

B. Axial-Flux Machines

The scaling laws for axial flux machines are similar to those of radial flux machines, with the key difference that not all the torque is generated at the tip radius. Assuming the average electromagnetic shear stress $\bar{\tau}$ is independent of radius, the power output of the electric machine is expressed as a function of the electric machine hub-to-tip radius ratio χ_E:

$$P_{E,axial} = \bar{\tau}\frac{2\pi}{3}(r_{ag}^3 - r_h^3)\Omega = \bar{\tau}\frac{2\pi}{3}(1-{\chi_E}^3)\mathbf{r_{ag}^3}\boldsymbol{\Omega} = \frac{1-{\chi_E}^3}{3(\frac{l}{r_{ag}})}P_{E,radial}. \tag{6}$$

The electric machine mass can similarly be written as

$$m_{E,axial} = \rho_{m,E}\pi(r_{ag}^2 - r_h^2)h_o = \rho_{m,E}\pi(1-{\chi_E}^2)(\frac{h_o}{r_{ag}})\mathbf{r_{ag}^3} = \frac{1-{\chi_E}^2}{2(\frac{l}{r_{ag}})}m_{E,radial}, \tag{7}$$

and the specific power of the electric machine Ξ_E then becomes

$$\Xi_{E,axial} = \frac{2(1-{\chi_E}^3)}{3(1-{\chi_E}^2)}\frac{\bar{\tau}}{\rho_{m,E}(\frac{h_o}{r_{ag}})}\boldsymbol{\Omega} = \frac{2(1-{\chi_E}^3)}{3(1-{\chi_E}^2)}\Xi_{E,radial}. \tag{8}$$

In the limit of a hub-to-tip radius ratio of 1 (axial flux machine approaching a radial flux machine), the expressions for specific power become equivalent.

While the above equations show both axial flux and radial flux machines scale similarly, the average EM shear stress in an axial flux machine is not directly comparable with that of the radial flux maching. Figure 5 illustrates how winding axial flux machine stators leads to the slot and surface current densities falling with radius. As the number of leads and current per lead are constant with radius, the maximum surface current density must occur at the machine hub, i.e.

$$K_s(r) = K_s(r = r_h)\frac{r_h}{r}. \tag{9}$$

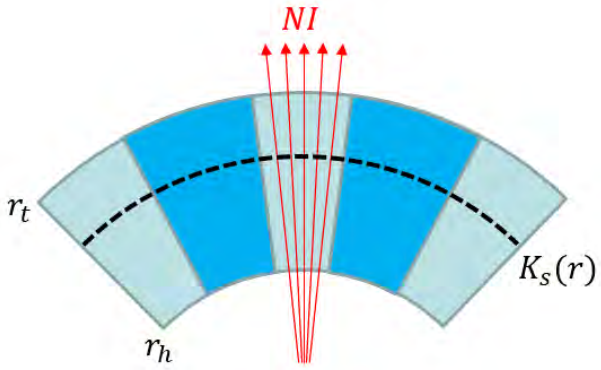

Fig. 5 Winding pattern of axial flux machines yields falling surface current densities with radius

Assuming that the surface current density in both axial flux and radial flux machines is limited by identical thermal constraints ($K_{s,radial} = K_{s,axial}(r = r_h)$), and that the gap flux density B_s in the axial flux machine is constant due to the proportional growth in magnet volume with radius, the current density limited EM shear stress for the axial machine can then be expressed as

$$\bar{\tau}_{axial}(r) = \bar{\tau}_{radial}\frac{r_h}{r}. \tag{10}$$

Integrating the EM shear stress along the air gap interface yields the expression for axial flux machine power

$$P_{E,axial} = \pi\bar{\tau}_{radial}\chi_E(1-\chi_E^2)r_{t,E}^3\Omega = \frac{\chi_E(1-\chi_E^2)}{2\frac{l}{r_{ag}}}P_{E,radial}. \tag{11}$$

Assuming the active element spatial density h_o/r_{ag} is equivalent between radial flux and axial flux machines, the ratio of specific powers can then be simply expressed as

$$\frac{\Xi_{E,axial}}{\Xi_{E,radial}} = \chi_E. \tag{12}$$

Figure 6 illustrates the trends in specific power ratio between axial flux and radial flux machines under the assumptions of uniform EM shear stress and current density-limited EM shear stress. In both scenarios radial flux machines outperform axial flux machines, with the margin increasing due to the more realistic current density-limited EM shear stress assumption. In machine architectures where the air gap flux falls with radius as well (e.g. induction rotors), axial flux machines would fall even further behind radial flux machines.

IV. Motor Drive Design for High Specific Power

A. Choice of Electric Machine Architecture

To meet the functional requirements listed earlier, an outer rotor arrangement is selected. This architecture yields a number of advantages, including placement of the rotor containment elements outside the air gap, and possible future integration with turbomachines (e.g. using the rotor outer surface as part of a compressor). Permanent magnets are chosen as the rotor element for their high efficiency, particularly important given the increased thermal management challenge of the rotor relative to the stator.

Four architectures comprising the possible combinations of two different stator and two different rotor configurations were considered in the design space exploration and are illustrated in 7: (1) Tooth and Slot Surface Permanent Magnet (PM), (2) Tooth and Slot Halbach Array, (3) Slotless Surface PM, and (4) Slotless Halbach Array. The tooth and slot is the more common of the two stator configurations, where teeth made from electrical steel concentrate the magnetic flux between rotor and stator, with the windings wrapped around the teeth. The slotless configuration eliminates the teeth, allowing for greater winding volume at the cost of an increased air gap. Additionally, electromagnetic shear stress is not limited by the magnetic saturation of the teeth in a slotless configuration, and can far exceed their tooth and slot

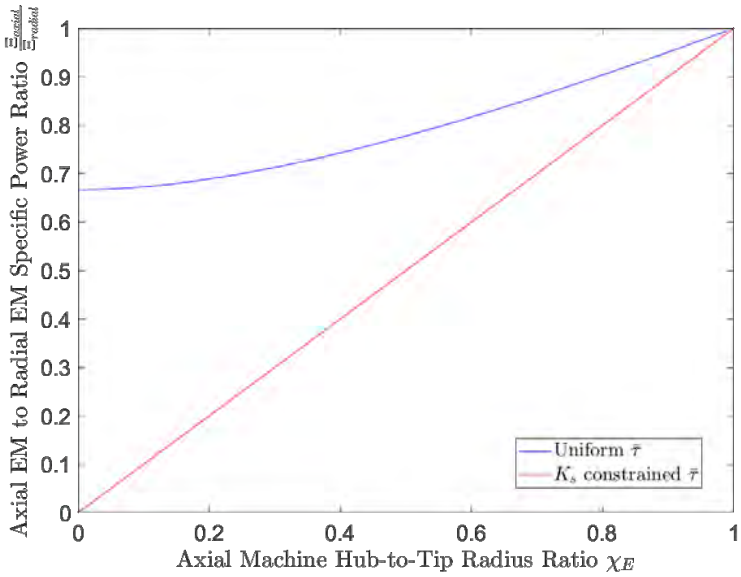

Fig. 6 Axial flux machines have lower specific power than radial flux ones with equivalent design parameters

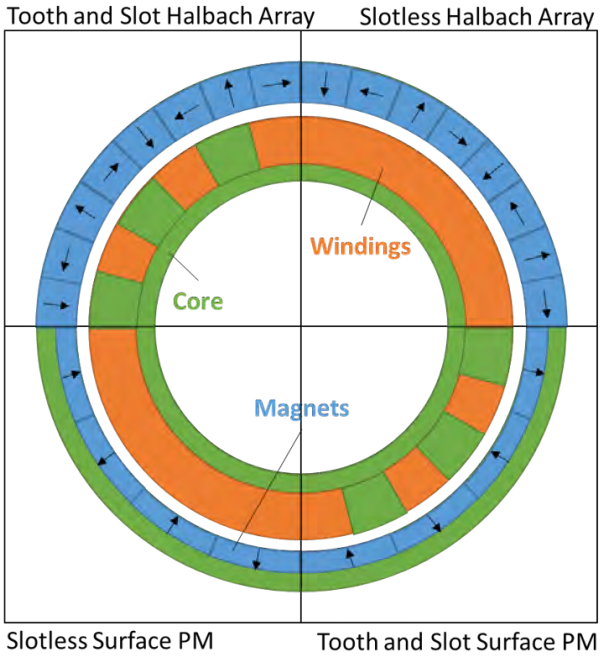

Fig. 7 Permanent magnet machine architecture options.

counterparts in superconducting machines. In the surface PM rotor configuration, a layer of electrical steel (referred to as the back iron) is placed on one side of the magnets (opposite of the air gap) to concentrate the magnetic flux. The Halbach array achieves the same effect without the back iron by rotating the orientation of the magnet pieces (adding azimuthal-facing pieces) such that the magnetic flux of the permanent magnets is cancelled on one side and reinforced on the other. The elimination of the rotor back iron enables further reduction in the load-bearing retaining sleeve, allowing for a thinner and lighter rotor at the same electromagnetic shear stress and mechanical speed. An important caveat, however, is that the benefit of the Halbach Array can only be realized above a minimum magnet thickness.

An outer rotor permanent magnet machine design framework was developed using reduced order models and

structural and thermal management constraints (details can be found in [3]. The design space exploration identified the tooth-and-slot, Halbach array architecture to maximize specific power across the power levels assessed.

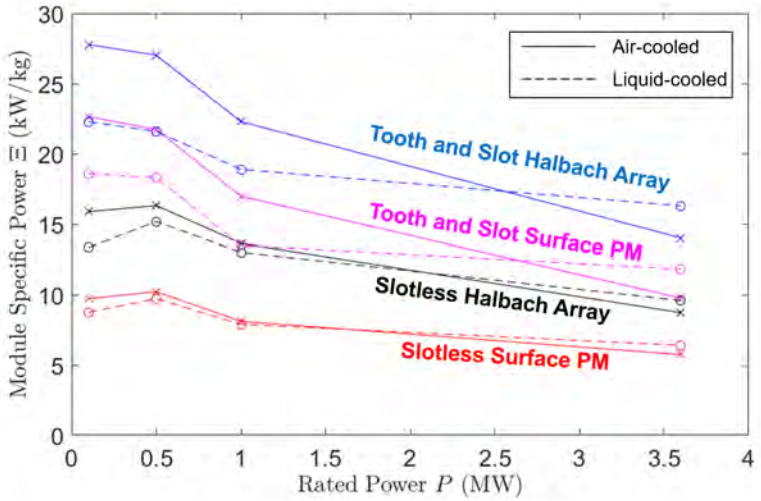

Fig. 8 Specific power trends of outer rotor PM machine architectures: tooth-and-slot Halbach array configuration outperforms across the power range assessed.

Figure 8 illustrates the trends in maximum module specific power against rated power for air-cooled and liquid-cooled machines of the four architectures considered. Each point corresponds to a machine design optimized over all electric machine design parameters for maximum module specific power. Tooth and slot architectures consistently outperform their slotless counterparts, and Halbach array architectures also outperform their surface PM counterparts. The teeth guide the magnetic flux in the stator and minimize the magnetic air gap, resulting in increased electromagnetic shear stress. Slotless machines in comparison tend to perform better at higher speeds and lower electromagnetic loading, where the magnetic air gap can be minimized by keeping the winding thickness low. The doubling of the estimated core loss as a measure of design conservatism and risk mitigation favors increased shear stress over increased mechanical speed, thus penalizing the performance of slotless machines more than their tooth-and-slot counterparts. The surface PM architecture requires additional rotor mass (back iron and additional rim thickness) to generate equivalent electromagnetic loading to their Halbach array counterparts, resulting in reduced specific power.

Liquid-cooled machines of all four architectures outperform their air-cooled counterparts at high power levels, where the tradeoff in increased thermal management system mass and power enables a greater reduction in electric machine mass. This is likely a result of the increased heat flux with rated power due to the cube-square law, making it increasingly difficult to air-cool machines at the same electromagnetic loading.

B. Choice of Power Electronics Architecture

A detailed topology comparison for high-speed motor drive applications [12] concluded that three single-phase full-bridge inverters yield superior specific power and efficiency relative to a three-phase bridge inverter and higher specific power than three-level active neutral point clamped (ANPC) inverters. Thus the full-bridge topology was selected to drive the high-specific power electrical machine.

Comparison of two-level (three-phase bridge, and three single-pase full-bridge) and three-level (ANPC) converters under an equal phase current ripple requirement showed that the increased efficiency of the three-level converter did not outweigh the associated mass penalty over a two-level converter. Further design space exploration narrowed down the optimum power conversion architecture to 10 separate 100 kW inverter sets distributed around the periphery of the electric machine, with each inverter unit consisting of three, single-phase full-bridge inverters. This is shown in Fig. 3 on the top right. The distributed conversion was adopted for a number of advantages, including improved weight and efficiency, packaging and cooling, modularity and maintainability, and flexibility for close integration of the power electronics with electric machine. More detail can be found in [9].

C. Integrated Motor Drive System Design Co-Optimization

The optimum motor drive design parameters were identified through a design space exploration utilizing a reduced-order modeling framework [3]. The performance metric is motor drive specific power, defined as the rated power minus system losses divided by the total system mass. The total system mass includes electromagnetic components, structural elements (load-bearing rotor), and heat exchangers. System losses include electrical, magnetic, and mechanical losses (windage and thermal management system power). A multi-stage compressor with an isentropic efficiency of 91% is assumed to provide the air flow to the thermal management system. This is similar to a turbo-electric propulsion configuration with the electrical machine embedded in the gas turbine aero-engine compression system.

The design tool yields estimates of machine mass and losses with a level of fidelity that captures performance trends with key design parameters. The design loop for each combination of input parameters is illustrated in Fig. 9

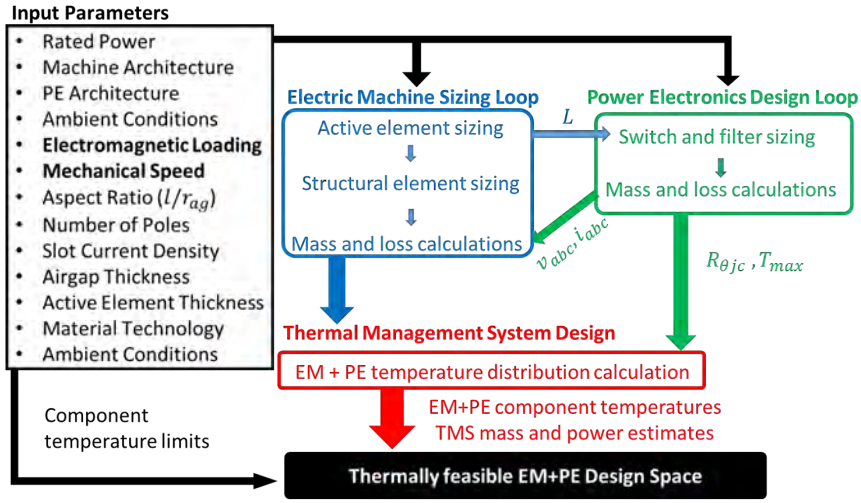

Fig. 9 Integrated motor drive design framework

The design space for a motor drive with the tooth-and-slot Halbach array configuration is shown in Figure 10. Each point in the chart represents a conceptual motor drive design at that combination of electromagnetic loading factor and mechanical speed, with all remaining parameters (pole count, electrical frequency, device switching frequency, etc) optimized. The non-dimensional electromagnetic loading factor is defined as the average electro-magnetic shear stress over the maximum shear stress under the constraint of magnetic saturation of the tooth tips, $\tau_{max} = B_c^2/16\mu_0$ [10].

The optimum design space lies on the boundary of the region of thermal feasibility, with a flat plateau over the range of 10000-12500 RPM. Along the plateau, trading electromagnetic loading for increased mechanical speed yields longer machines with smaller tip radii. The reduction in electromagnetic loading trades copper losses for core losses, which have a shorter conduction path to the cooling surfaces. More detail on design space exploration and optimization can be found in [5] and [3].

V. MW-Class Integrated Motor Drive Performance Estimates

The 1 MW motor drive was designed to operate at 12500 RPM and a rated torque of 765 Nm. The breakdown of masses and losses of a single demonstrator unit are summarized in Tables 1 and 2 respectively, and illustrated as pie charts in Figs. 11 through 16. In the absence of a singular definition of what masses and losses should be accounted for in defining the specific power of a motor drive, several definitions and numbers for the demonstrator are described below.

- **Electric Machine Specific Power: 17.1 kW/kg.** Performance metric for comparison with other motors or generators. Accounts for electric machine masses and losses only.

- **Power Electronics Specific Power: 20.2 kW/kg.** Performance metric for comparison with other inverters or rectifiers. Accounts for power electronics masses and losses only.

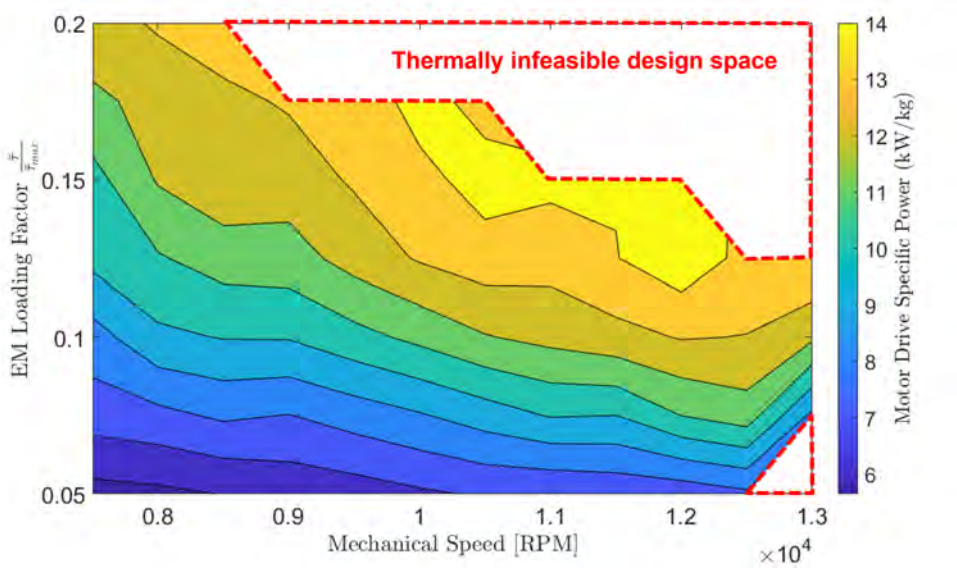

Fig. 10 Design space of tooth-and-slot Halbach array outer rotor machine configuration and integrated power electronics.

- **Motor Drive Specific Power: 8.3 kW/kg.** Accounts for masses and losses of electric machine and power electronics, including the 'loss' of power required to operate the thermal management system. System-level performance metric that is optimized for during the demonstrator design process.

- **Application Specific Power: 3.1 kW/kg.** Accounts for all demonstrator masses and losses, including those of components which are not optimized for minimum mass (e.g. shielding constructed from A36 steel as a method of containing fragments in case of rotor failure). Performance metric of the motor drive demonstrator unit as an application.

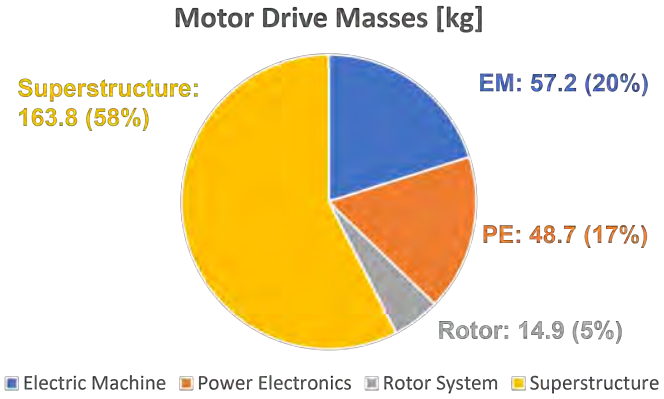

Fig. 11 Mass breakdown of motor drive by subsystem

The individual component masses are calculated from detailed CAD models which were used to produce manufacturing drawings. Losses are estimated from a combination of empirical models, experimental measurements, and factors of conservatism. For example, the core losses are estimated by taking experimentally-measured toroid loss data (in W/kg) for operating frequency and peak flux density, and multiplying by the mass of the core steel (in effect making a conservative assumption that all parts of the stator are fully saturated), and then doubled for a safety factor of 2.

Component	Mass (kg)	Component	Mass (kg)
Electric Machine		**Rotor System**	
Stator teeth	11.3	Forward end bell	3.5
Stator back iron	8.4	Aft end bell	0.5
Axial windings	4.2	Driveshaft	0.8
End windings	1.7	Rotor fasteners	0.4
Permanent magnet	14.6	Forward and aft bearings	2.4
Rotor drum	10.6	Bearing locknut and washers	0.1
Heat exchanger	6.4	Dampers	0.1
Total	**57.2**	Bearing housing and fasteners	7.1
Power Electronics		**Total**	**14.9**
FETs	3.8	**Electric Machine Superstructure**	
Drivers	1.9	Forward frame (including alignment cage)	26.5
HF capacitors	2.6	Aft frame (including spindle)	23.5
Circuit board	4.9	Shielding	77.2
Heat exchangers	2	Forward and aft legs	33.1
Leads between EM and PE	0.5	180 degree bend	0.5
PE frame	33.0	Superstructure fasteners	3.0
Total	**48.7**	**Total**	**163.8**

Table 1 Breakdown of estimated motor drive masses

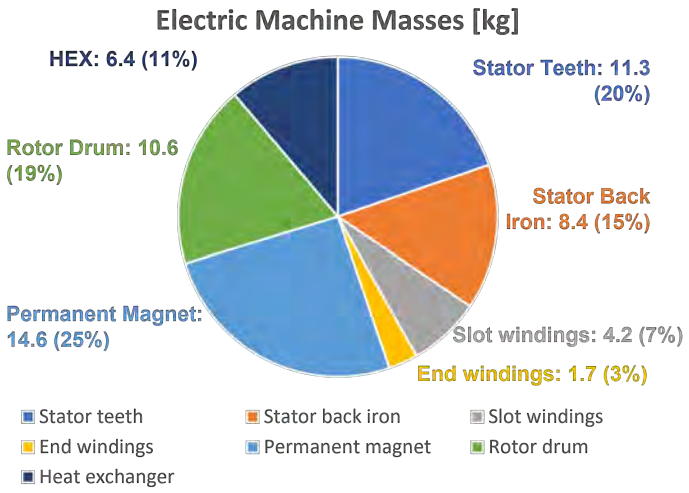

Fig. 12 Mass breakdown of electric machine by component

The mass of the compressor is not considered as part of thermal management system, as it is assumed the motor drive would be cooled with bleed air from a gas turbine in application. The thermal management system (TMS) power component of the losses is the additional mechanical power input to the compressor to supply the cooling flow to the demonstrator. This mechanical power is calculated as the work input to a compressor with 91% isentropic efficiency to restore the total pressure of the exhaust flow to ambient conditions. The cooling flow pressure losses are estimated with a combination of empirical models and CFD.[†]

[†]The pressure losses in the power electronics flow are not estimated but assumed to be equivalent to those of the electric machine as a conservative estimate.

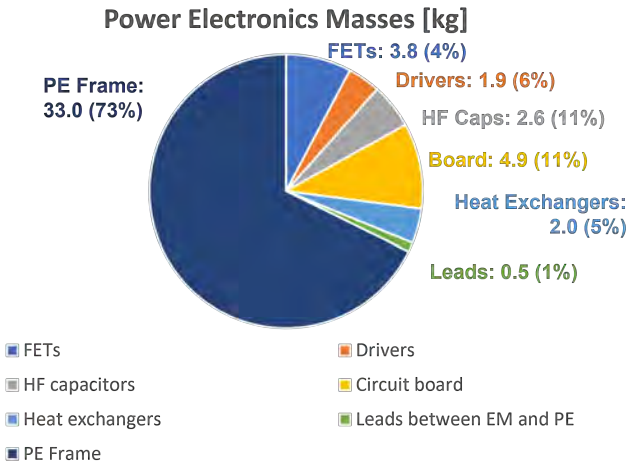

Fig. 13 Mass breakdown of power electronics by component

Component	Losses [kW]	Component	Losses [kW]
Electric Machine		**Power Electronics**	
Core	8.8	FET conduction	3.8
Permanent magnets	1.8	FET switching	11.8
Airgap rotor windage	2.0	Drivers	0.1
Outer rotor windage	2.3	HF Capacitors	1.2
Fundamental winding	6.9	LF Capacitors	0.1
HF winding	1.1	Leads between EM and PE	0.6
HF core	0.3	**Total**	**17.6**
Total	**23.7**	**Thermal Management**	
Bearings		EM cooling flow	59.5
Bearing friction	0.1	PE cooling flow	23.4
Total	**0.1**	**Total**	**82.9**

Table 2 Breakdown of estimated motor drive losses at rated power

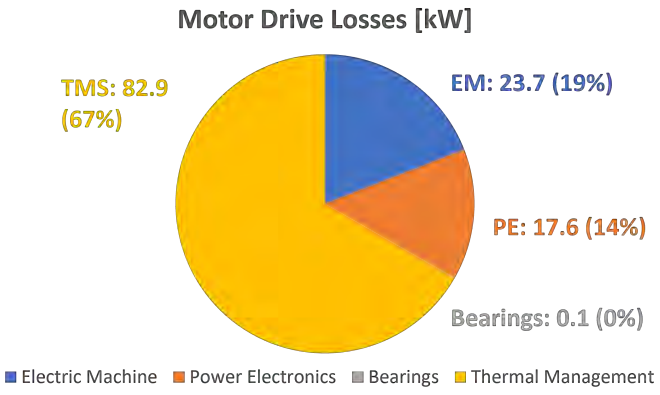

Fig. 14 Loss breakdown of motor drive by subsystem

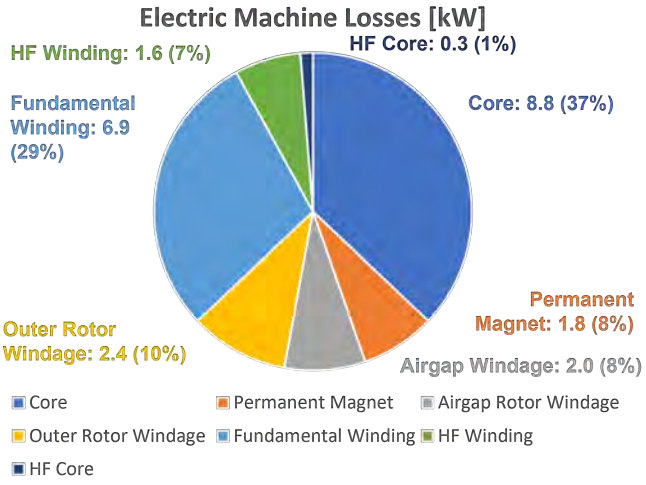

Fig. 15 Loss breakdown of electric machine by component

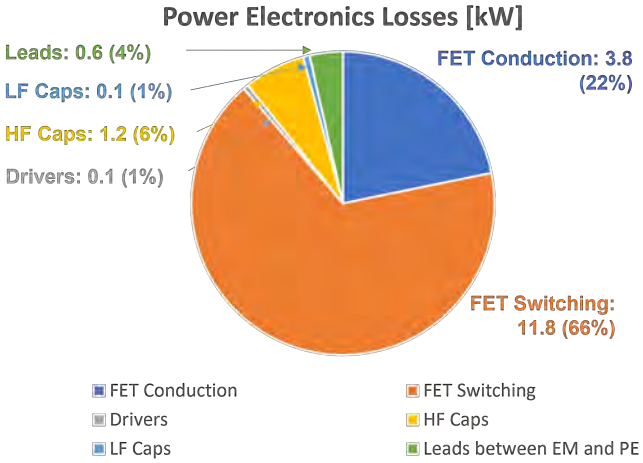

Fig. 16 Loss breakdown of power electronics by component

Nominal operation of the air cooling system provides a 23°C temperature margin for the winding hotspot to accommodate possible loss underestimates, which means the system can accommodate an additional 50% (or 4.4 kW) of core losses before the winding hotspot temperature is reached. Should the losses be overestimated and the winding hotspot temperature found to be cooler than predicted, the cooling flow can be reduced to minimize the TMS power losses and improve demonstrator and application specific power. Removing the 23°C temperature margin by reducing the cooling flows would reduce the TMS power requirement by 68% or 56.5 kW and increase the module efficiency by 0.05 pts.

VI. Thermal Management System Performance

The air cooled thermal management system is comprised of three cooling flow paths illustrated in Figure 17. To estimate cooling performance a flow resistor network is implemented as shown in Figure 18. The air cooling system is suction-driven by a downstream compressor. Compared to a upstream pump-driven system, this setup trades the advantage of a lower inlet air temperature for the motor drive (without utilizing a pre-cooler) at the cost of being limited in allowable pressure drop. The mass flow rates through three different cooling paths are controlled by a combination of the compressor speed and the settings on air gap and power electronics flow control valves.

The exhaust system and power electronics cooling system were designed to be compatible with the DeLaval

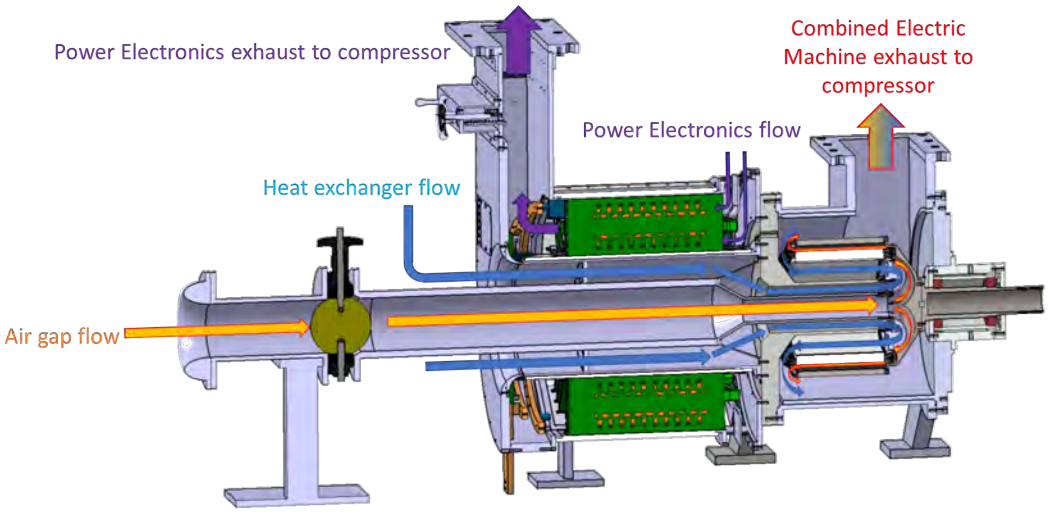

Fig. 17 Cooling air flow paths of the thermal management system for the motor drive

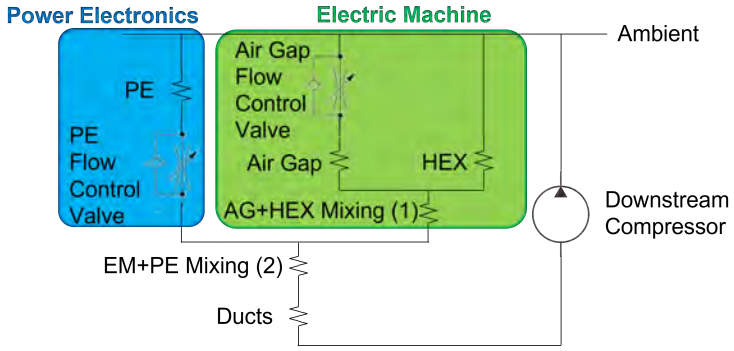

Fig. 18 Demonstrator flow resistor network captures all major sources of flow pressure losses, and is used to estimate valve and compressor speeds necessary for operation

compressor and air system of the MIT Gas Turbine Laboratory. The power electronics are cooled by off-the-shelf heat exchangers, with a nominal mass flow per unit of 0.44 kg/s set by a target average flow velocity of 4 m/s over the boards. The pressure losses of the power electronics cooling loop are not estimated but expected to be lower than the electric machine flow. The inverter boards were experimentally evaluated at rated power and the component temperatures were found to be well below their limits when cooled with externally driven fans supplying an identical flow velocity. More detail can be found in the companion paper on power electronics [9]

The various stations of the electric machine cooling flows are illustrated in Figure 19 and described in Table 3. The air gap and heat sink flows mix between stations 6 and 7, and the electric machine and power electronics cooling flows mix between stations 7 and 8.

As shown in Figure 20 on the left, the endbell forms the gas path for the air gap coolant flow (red arrow) and is carefully tailored to provide effective cooling of the end turns. The inset illustrates adequate distribution of cooling air around the wire leads. The heat exchanger coolant flow (blue arrow) is illustrated in the right figure where the bend is designed so as to redistribute flow for improved thermal performance. The coolant flow profile is skewed on purpose to yield higher velocities on the outer radius for enhanced convection heat transfer to cool the stator. The design was assessed in a heat exchanger experiment and the flow measuremens agree well with the CFD simulations.

The estimated station-average total pressure, temperature, and Mach number of the cooling flows are summarized in Figure 21. The pressure drop in the heat sink and across the S-bend between stations 1 and 2 is a conservative estimate based on measurements from the heat sink experiments discussed in the companion paper on the thermal management system [8]. The cooling flows reach high speeds at several locations: Mach 0.5 in the air gap and Mach 0.45 just

upstream of the 180 degree bend into the heat exchanger. This requires accounting for compressibility on heat transfer and pressure losses in the models used.

	Location	
Station Number	**Airgap Flow**	**Heat Exchanger Flow**
1	Inlet	Inlet
2	Downstream of FCV	Downstream of S-bend
3	Inlet to 180 degree bend	Inlet to 180 degree bend
4	Inlet to forward end turns	Inlet to heat exchanger
5	Inlet to air gap	Inlet to rear end turns
6	Air gap exit	Rear end turns exit
7	Electric machine exhaust	
8	Demonstrator combined exhaust	
9	Inlet to downstream compressor	

Table 3 Description of electric machine cooling flow stations

The exhaust flow conditions are checked against the map of the downstream compressor shown in Fig. 22) to ensure operability of the air cooling system. Limits on stall margin (in red) and compressor speed (in purple) are further imposed as measures of conservatism. The nominal operating point of the air cooling system is identified as the combination of FCV and compressor speed settings that yields the lowest electric machine hotspot temperatures. At this point, the commanded mass flows through the heat sink and the air gap are 0.78 kg/s and 0.34 kg/s per electrical machine unit.

With this thermal management system in place, Fig. 23 demonstrates successful air cooling of the electric machine at the nominal operating point. The winding hotspot temperature is estimated at 159°C, 21 degrees below the insulation temperature limit, and the magnet hotspot temperature of 72°C is far below demagnetization temperatures of 200°C. More detail on the experimental demonstration of the thermal management system can be found in a companion paper [8].

VII. Design for Manufacturing and Assembly

Careful consideration of the manufacturing and assembly processes was incorporated in the detailed design of the motor drive demonstrator. This includes additional material property requirements and design features, two examples of which are briefly described in this section. More detailed discussion of mechanical, structural and rotordynamic integrity can be found in the companion paper [6].

A. Stator Slot Potting

Potting is used to fill the gaps in the slots of the electric machine stator, providing additional electrical insulation and aiding in heat conduction between the windings and laminations. High thermal conductivity is desirable for the latter purpose, and can be achieved with the inclusion of metal particulates in the epoxy. However, to avoid air pockets and voids (which would drastically increase local thermal resistance and create hotspots), it is critical that the potting fully fills the slot during the Vacuum Pressure Impregnation (VPI) process. The potting material must have sufficiently low viscosity and a long working time to accomplish this, and both parameters were found to trade against thermal conductivity during the material search process.

As a result of this constraint, CoolTherm EP-2000 was selected for the potting material over the CoolTherm SC-320 SLW despite its lower thermal conductivity (1.9 W/mK for EP-2000 compared with 3.2 W/mK for SC-320 SLW) due to its lower dynamic viscosity when mixed (1900 cP for EP-2000 and 22500 cP for SC-320 SLW) maximizing the chances in attaining full slot penetration during the VPI process.

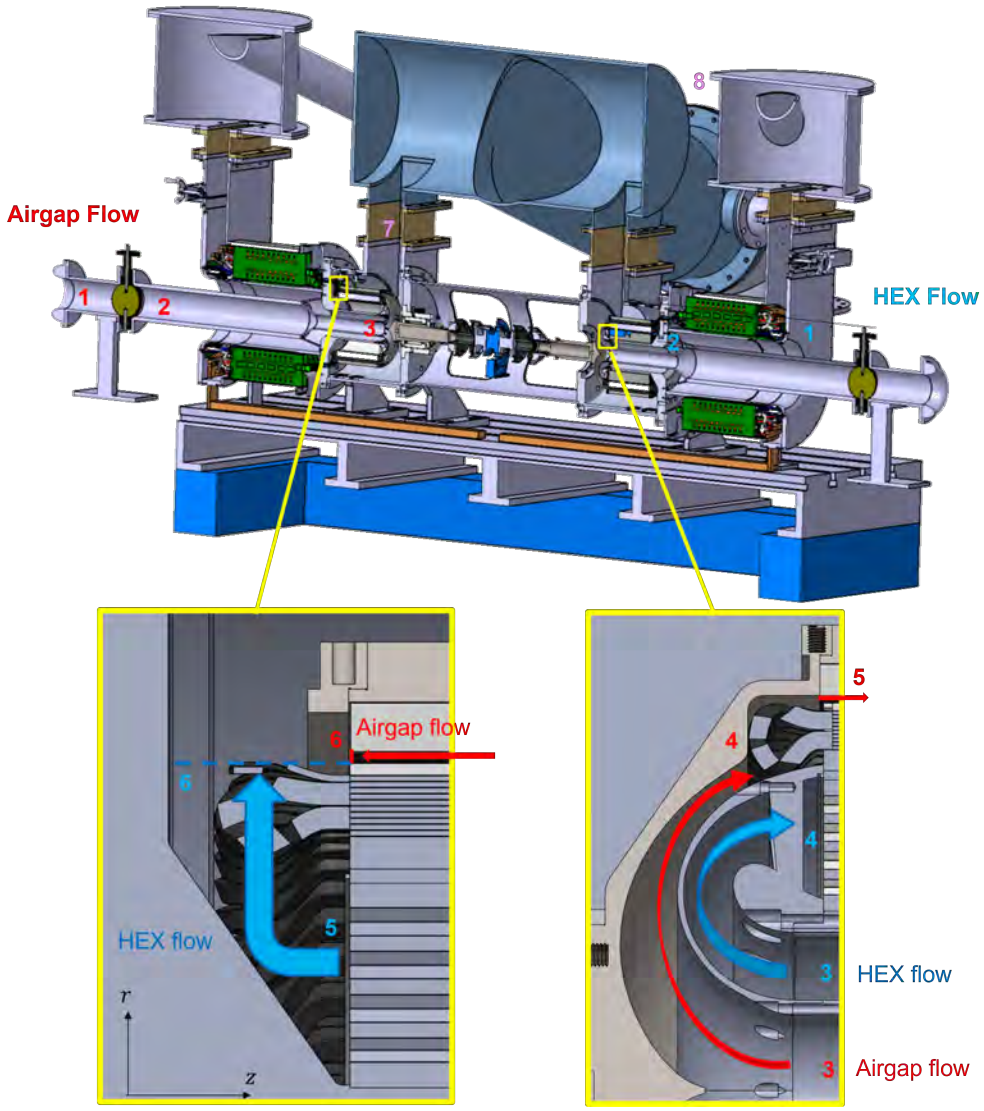

Fig. 19 Electric machine cooling flow stations shown for back-to-back motor-generator demonstrator setup at the MIT Gas Turbine Laboratory

B. Alignment Cage for Machine Assembly

The attractive magnetic forces between electric machine rotor and stator are significant (even when the stator is unenergized), and present a risk of collision between the two components during the assembly process. These collisions can result in damage to rotor and stator, such as chipping of the brittle magnets that degrade machine performance. The risk of collision is typically prevented through the use of Teflon skids between rotor and stator during assembly process. The Teflos skids are then removed after assembly is completed.

Removing the strips post-assembly is challenging with the overhung rotor architecture, as the long Teflon skids would have to be nursed out of the comparatively narrow gap between the aft end of the rotor and the aft frame. It would also be impossible to insert the skids back into the air gap in this manner during disassembly. Access to the Teflon skids can be improved by cutting ports in the forward end bell through which the skids are inserted and removed, but this compromises the structural integrity of the forward end bell (which transfers the full machine torque between driveshaft and rotor drum).

An alignment cage presented in Fig. 24 was conceived to prevent rotor-stator collision during assembly and disassembly without the complications associated with the Teflon strips. The alignment cage is part of the forward frame, which is itself rigidly connected to the bearing housing unit (and subsequently the rotor). The radial gap between

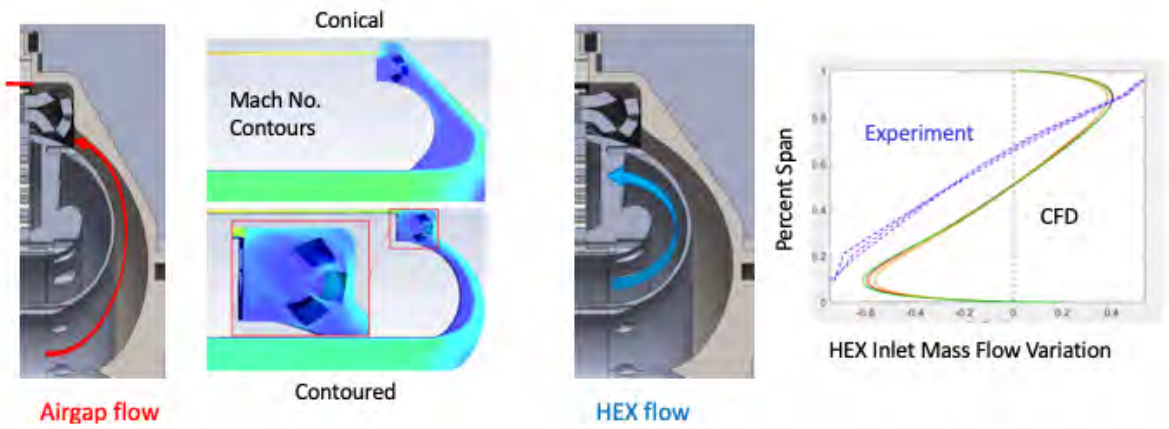

Fig. 20 End bell contouring for enhanced end-turn cooling (left), and tailored heat exchanger bend to redistribute flow for improved thermal performance (right)

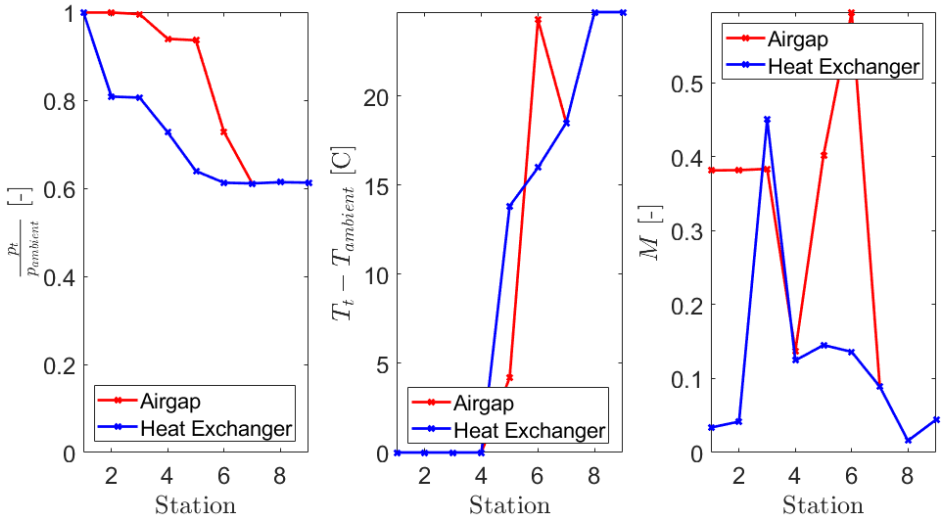

Fig. 21 Electric machine cooling flow states: stagnation pressure drop (left), temperature change (center), and Mach number (right)

the alignment cage and shielding is smaller than rotor-stator airgap, meaning that any misalignment during the assembly process (that might be introduced by the stator-rotor attractive forces, for example) would cause the cage and shielding to collide before rotor and stator make contact. Figure 25 illustrates the installation process, with the rotor assembly lowered onto the stator assembly and initial points of contact circled in red. The disassembly process occurs in reverse, with the alignment cage performing the same role in preventing collisions. As the alignment cage remains in place during operation of the demonstrator, it is assessed in FEA to ensure its natural frequencies are sufficiently separated from the operating speed.

VIII. Scaling of the Integrarted Motor Drive to Higher Power Levels

The 1 MW motor drive system is optimized for operation at its structural, magnetic, and thermal limits. To address scaling the design to higher rated power levels, such as multi-megawatt systems that might be used as generators on single aisle turbo-electric aircraft, the electric machine scaling laws introduced earlier are briefly revisited.

Equation 4 shows specific power scales as the inverse of the square root of rated power, which suggests that simply

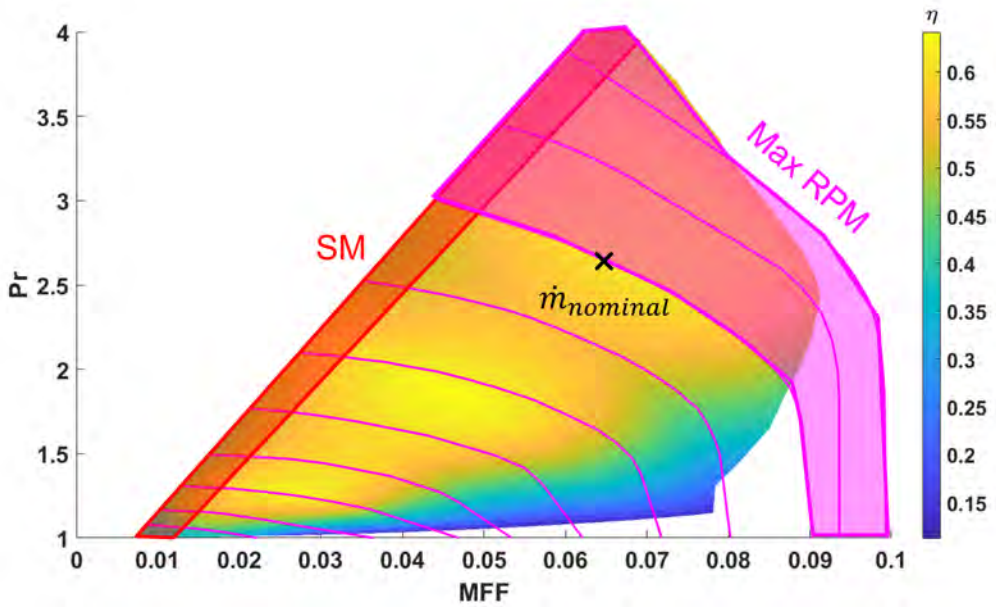

Fig. 22 Performance map of DeLaval compressor and air system at the MIT Gas Turbine Laboratory

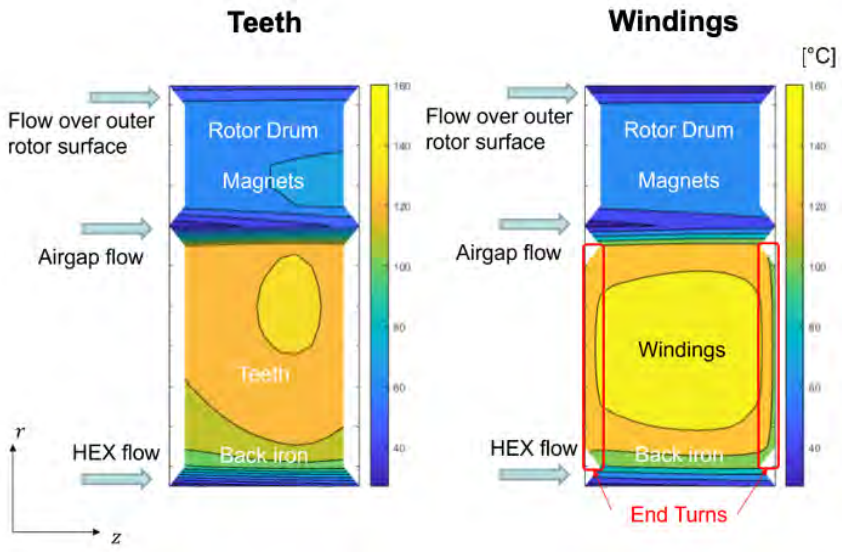

Fig. 23 Electric machine temperature distribution at nominal operating point: the winding temperature hotspot yields a 50% core loss margin (on top of doubling the core loss safety factor)

scaling the demonstrator up to 3.6 MW would cause the specific power to fall by half, which would not meet NASA performance targets. To avoid this, improvements to the critical design parameters (electromagnetic shear stress, tip speed, machine aspect ratio, and material technology) must be made.

Electromagnetic loading can be increased with more effective cooling systems, including the switch from air-cooling to liquid-cooling. The conceptual trade studies presented earlier suggest that the additional mass and loss penalties of a liquid cooling system enable superior system performance at the multi-megawatt level. The performance of the air-cooling system can also be extended through the use of pre-coolers, reducing the inlet temperature of the air and the

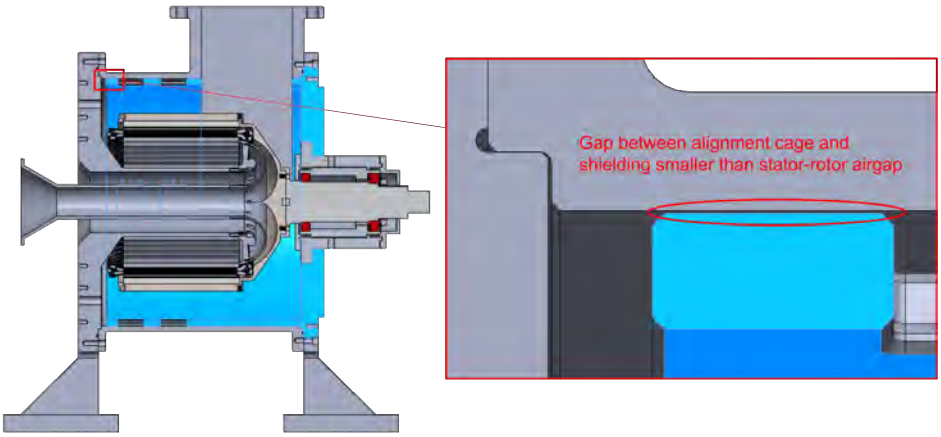

Fig. 24 Alignment cage to avoid collision between rotor and stator during assembly and disassembly is part of forward frame (highlighted in blue)

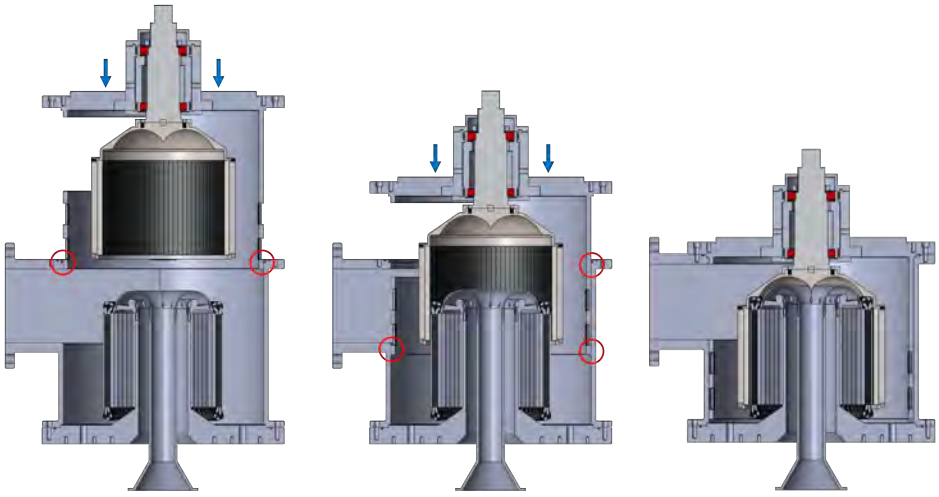

Fig. 25 Rotor-stator assembly process (initial points of contact between cage and shielding circled in red)

hotspot temperature proportionally.

Increasing the tip speed of the demonstrator is particularly challenging. The titanium alloy used for the rotor drum (Ti-6Al-4V) possesses one of the highest strength-to-weight ratios of all metals, making it difficult to improve upon from a perspective of structural integrity. Wrapping the rotor drum with a carbon-fibre shell is a possible solution, but it eliminates the possibility of using the outer surface as part of the compressor. Additionally, while the carbon-fibre shell is strong in resisting centrifugal loads, it is less effective in improving the flexural rigidity of the rotor. This exacerbates the challenge of maintaining the electric machine air gap during operation, especially under the increased unbalance forces associated with increased tip speed.

Improving machine aspect ratio will require addressing multiple operability challenges and likely changes in the overall rotor architecture. A longer machine would result in a lengthened spindle and exacerbate the spindle vibration challenge for the overhung rotor architecture. The increased length would also be accompanied with larger coolant pressure losses and an increase in thermal management system power requirements. Switching to an alternative bearing layout may be necessary, and the associated problems of routing the cooling flows and maintaining bearing operability must be addressed.

In addition to the many material and manufacturing technology improvements beneficial to electric machines in general (such as lamination steels with superior saturation flux density and core losses), high temperature materials are of particular interest for aircraft propulsion applications. Increasing machine operating temperatures allows for bleed air from later stages of the compressor to be used, increasing the allowable coolant pressure losses and thus cooling

capability. For liquid-cooling systems, the heat produced in conventional electric machines is typically low quality (as it is generated at comparatively low temperatures of ~200°C due to material temperature limits on potting and insulation), and is thus expensive to reject from an aircraft's oil-to-air heat exchangers. High temperature electric machine materials thus present not only the opportunity for machine-level improvements due to the increase in electromagnetic loading enabled, but also to mitigate the system-level penalties of mass and loss associated with heat rejection to atmosphere.

IX. Summary and Conclusion

A 1 MW integrated motor drive is in development, with key technologies identified and demonstrated. These include (but are not limited to) successful operation of the Halbach rotor at design speed in a spin pit, and operation of the full-bridge inverters at rated power with >98.3% efficiency. The demonstrator outcomes are scalable and applicable to a wide variety of applications in transportation, power generation, and industry. For propulsion applications specifically, possibilities include the installation of an integrated motor or generator on board existing gas turbines for power assist in the near term and the development of motor-fan concepts for distributed propulsion in the long term.

The integrated motor drive demonstrator will soon be commissioned at the MIT Gas Turbine Laboratory. Detailed mapping of the performance of the motor, generator, and power electronics up to a rated power of 1 MW will be performed. Machine operation will be assessed as both motor and generator following torque/load control strategies for the generator and speed control strategies for the motor. The commissioning process will also include investigation of system dynamic behavior and stability, such as the effectiveness of the thermal management system under transient operation conditions.

Acknowledgments

This project is funded by Mitsubishi Heavy Industries which is gratefully acknowledged. Special thanks go to Koichiro Iida, Mikito Sasaki, and Masahiko Ezumi for their technical support and collaboration. The authors would like to also thank former team member Dr. Aidan Dowdle for his contributions to the electromagnetic design of the the motor drive system. Charlotte Gump is also acknowledged for her support and help with the heat sink experiments.

References

[1] Jansen, R., Bowman, C., Jankovsky, A., Dyson, R., and Felder, J., "Overview of NASA Electrified Aircraft Propulsion Research for Large Subsonic Transports," *53rd AIAA/SAE/ASEE Joint Propulsion Conference, AIAA Propulsion and Energy Forum*, 2017, pp. 8–27. URL `https://ntrs.nasa.gov/archive/nasa/casi.ntrs.nasa.gov/20170012222.pdf`.

[2] El-Refaie, A., and Osama, M., "High specific power electrical machines: A system perspective," *2017 20th International Conference on Electrical Machines and Systems (ICEMS)*, 2017, pp. 1–6. https://doi.org/10.1109/ICEMS.2017.8055931.

[3] Chen, Y. K., "Technology Demonstration of a Megawatt-Class Integrated Motor Drive for Aircraft Propulsion," Ph.D. thesis, Massachusetts Institute of Technology, 2023.

[4] ABB, "ACS6000 Medium Voltage Drive," Brochure, 2015. URL https://library.e.abb.com/public/93e7987509e7f4d048257e12004ce8f5/ACS6000$%$20Product$%$20brochure_low-res_Rev$%$20G.pdf.

[5] Dowdle, A., "Design of a High Specific Power Electric Machine for Turboelectric Propulsion," Ph.D. thesis, Massachussets Institute of Technology, 2022.

[6] Chen, Y., Spakovszky, Z. S., Greitzer, E. M., Cordero, Z. C., and Cuadrado, D. G., "High Speed Rotor System for a Megawatt-Class Integrated Motor Drive Technology Demonstrator," AIAA/IEEE Electric Aircraft Technologies Symposium (EATS), 2023. Extended Abstract Submission.

[7] Andersen, H., Spakovszky, Z. S., Lang, J. H., Kirtley, J. L., and Greitzer, E. M., "High Specific Power Permanent Magnet Synchronous Machine for a Megawatt-Class Integrated Motor Drive Technology Demonstrator," AIAA/IEEE Electric Aircraft Technologies Symposium (EATS), 2023. Extended Abstract Submission.

[8] Chen, Y., Spakovszky, Z. S., Greitzer, E. M., Cordero, Z. C., Cuadrado, D. G., and Gump, C., "Novel Channel-type Heat Exchanger for a Megawatt-Class Integrated Motor Drive Technology Demonstrator," AIAA/IEEE Electric Aircraft Technologies Symposium (EATS), 2023. Extended Abstract Submission.

[9] Qasim, M. M., Otten, D. M., Spakovszky, Z. S., Lang, J. H., Kirtley, J. L., and Perreault, D. J., "Design and Optimization of an Inverter for a One-Megawatt Ultra-Light Motor Drive," AIAA/IEEE Electric Aircraft Technologies Symposium (EATS), 2023. Extended Abstract Submission.

[10] Smith, J. L., Jr., Kirtley, J. L., Gerstman, J., and Rumore, F. C., "Assessment of the Technology of Electric Transmission Subsystems," *Institute for Defense Analyses Paper IDA-P-1278*, 1978.

[11] Farve, N. N., "Design of a Low-Mass High-Torque Brushless Motor for Application in Quadruped Robotics," Ph.D. thesis, Massachusetts Institute of Technology, 2012.

[12] Qasim, M. M., Otten, D. M., Lang, J. H., Kirtley, J. L., and Perreault, D. J., "Comparison of Inverter Topologies for High-Speed Motor Drive Applications," *2021 IEEE 22nd Workshop on Control and Modelling of Power Electronics (COMPEL)*, 2021, pp. 1–8. https://doi.org/10.1109/COMPEL52922.2021.9645956.